INTERNATIONAL JOURNAL FOR NUMERICAL METHODS IN ENGINEERING
Int. J. Numer. Meth. Engng 2004; 00:1–22 Prepared using nmeauth.cls [Version: 2002/09/18 v2.02]

Inverse geometry heat transfer problem based on a radial basis functions geometry representation

Marcial Gonzalez and Marcela B. Goldschmit*†

Center for Industrial Research, FUDETEC
Dr. Jorge A. Simini 250, B2804MHA, Campana, Buenos Aires, Argentina

SUMMARY

We present a methodology for solving a nonlinear inverse geometry heat transfer problem where the observations are temperature measurements at points inside the object and the unknown is the geometry of the volume where the problem is defined. The representation of the geometry is based on radial basis functions (RBFs) and the nonlinear inverse problem is solved using the iteratively regularized Gauss-Newton method. In our work, we consider not only the problem with no geometry restrictions but also the bound-constrained problem.

The methodology is used for the industrial application of estimating the location of the 1150°C isotherm in a blast furnace hearth, based on measurements of the thermocouples located inside it. We validate the solution of the algorithm against simulated measurements with different levels of noise and study its behavior on different regularization matrices. Finally, we study the error behavior of the solution. Copyright © 2004 John Wiley & Sons, Ltd.

key words: heat conduction; inverse geometry problem; radial basis functions; iteratively regularized Gauss-Newton method; blast furnace hearth

1. INTRODUCTION

Inverse heat transfer problems are important for various industrial applications. The purpose of inverse heat transfer problems is to recover causal characteristics from information about the temperature field. Causal characteristics of heat transfer are boundary conditions and their parameters, initial conditions, thermophysical properties, volumetric heat sources as well as geometric characteristics of the studied object.

In this paper, we present a methodology for solving a nonlinear inverse geometry heat transfer problem where the observations are temperature measurements at points inside the object and the unknown is the geometry of the volume where the problem is defined. In Section 2, we

*Correspondence to: Center for Industrial Research, FUDETEC. Dr. Jorge A. Simini 250, B2804MHA, Campana, Buenos Aires, Argentina.
†E-mail: sidgld@siderca.com

Contract/grant sponsor: SIDERAR (Argentina)

formally define the general inverse heat transfer problem and describe the finite element model developed to solve the direct heat transfer problem.

There are a number of publications dealing with industrial applications of inverse geometry problems (IGPs). Wawrzynek et al.[1] have combined IGPs with infrared tomography in order to study non-destructive evaluation of surface damages in concrete structural elements. Park et al.[2] have developed a model to identify the boundary shape of a domain dominated by natural convection, which can be potentially applied in the determination of a phase change isotherm in the Bridgman crystal growth of semiconductor materials. Kwag et al.[3] have estimated the phase front motion of ice by applying an IGP; this model was used by the authors for controlling and monitoring a latent heat energy storage system. Huang et al.[4] have proposed to use an IGP to estimate the shape of frost growth on an evaporating tube by using temperature readings. Ganapathysubramanian et al.[5] have presented a framework to evaluate the shape sensitivity of finite thermo-inelastic deformations and have applied the method to the design of open- and closed-die forging processes.

It is well-known that inverse problems are typically ill-posed in the sense that small observation perturbations can lead to big errors in the solution. Such problems do not fulfill Hadamard's postulates of well-posedness [6, 7], where one of the following properties does not hold: a solution exists for all admissible data, the solution is unique, the solution depends continuously on the data. Therefore, regularization methods have to be applied in order to guarantee a stable solution.

Several regularization methods have been used in the literature to handle nonlinear ill-posed problems [6, 7] by replacing the original ill-posed problem with a well-posed approximated problem. Iterative regularization appears to be one of the most efficient approaches for the construction of stable algorithms for solving nonlinear inverse problems [7]. Among this class of methods, we use the iteratively regularized Gauss Newton method [8, 9, 10, 11]. In Section 3, we formulate the inverse geometry problem considering the case of a linear combination of several regularization matrices and a bound constrained problem with geometry restrictions.

The estimated geometry of the object is described by polyharmonic radial basis functions (RBFs) from a set of interpolation points defined by a set of parameters which are actually the inverse geometry problem unknowns. RBFs are used both because they impose few restrictions on the geometry of the interpolation points which do not need to lie on a regular grid, and because they provide a smooth interpolation [12, 13, 14, 15, 16, 17].

Radial basis functions are a recent tool for interpolating data and have been used in many areas. Perrin et al. [14] and Carr et al. [13] have used RBFs in medical imaging; Turk et al. [18] and Carr et al. [12] have modeled surfaces implicitly with RBFs in computer graphics; Kansa [16, 17] has introduced the RBFs method for solving partial differential equations; and Belytschko et al. [19] have developed a structured finite element method for solids which uses RBFs to implicitly define surfaces. Frankle [15] has found that the RBFs are the best 2D scheme among 29 different methods for scattered data interpolation.

In Section 4, we present the parametrization of the geometry, an introduction to RBFs interpolation and a description of a simple bidimensional remeshing algorithm developed by us.

The industrial problem to be solved in this paper is the estimation of the blast furnace hearth wear. One of the most critical parts of the blast furnace is its hearth, which cannot be repaired or relined without interrupting its production for a long time. Therefore, the blast furnace campaign is mainly limited by the hearth refractory wear which is produced

by thermo-chemical solution and thermo-mechanical damage [20]. Since direct measurements of the remaining lining thickness are impossible to be obtained, we use information about the thermal state of the blast furnace hearth to estimate the erosion profile. Moreover, the location of the 1150°C isotherm is particularly useful because it represents a potential limit on the penetration of liquid iron into the hearth wall porosity (1150°C is the eutectic temperature of carbon saturated iron [20]).

In Section 5, we develop the industrial application of estimating the location of the 1150°C isotherm in a blast furnace hearth, based on measurements of thermocouples located inside it [21, 22, 23, 24]. Further, we validate the solution of the algorithm against simulated measurements with different levels of noise and study its behavior on different regularization matrices. We analyze the problem with no geometry restrictions but also the bound-constrained problem. Finally, we study the error behavior of the solution.

The last Section deals with the work conclusions.

2. DEFINITION OF THE GENERAL PROBLEM

Consider a general steady-state heat transfer problem defined on an arbitrary volume (Ω) which has a fixed boundary ($\partial\Omega_n$) where natural boundary conditions are applied, and an unknown boundary ($\partial\Omega_T$) where a known temperature is applied. The shape and number of materials that the volume Ω contains will depend on the location of the boundary $\partial\Omega_T$. As shown in Figures 1.a and 1.b, since the materials are on fixed positions, different locations of the boundary $\partial\Omega_T$ cause different shapes of materials M3 and M4.

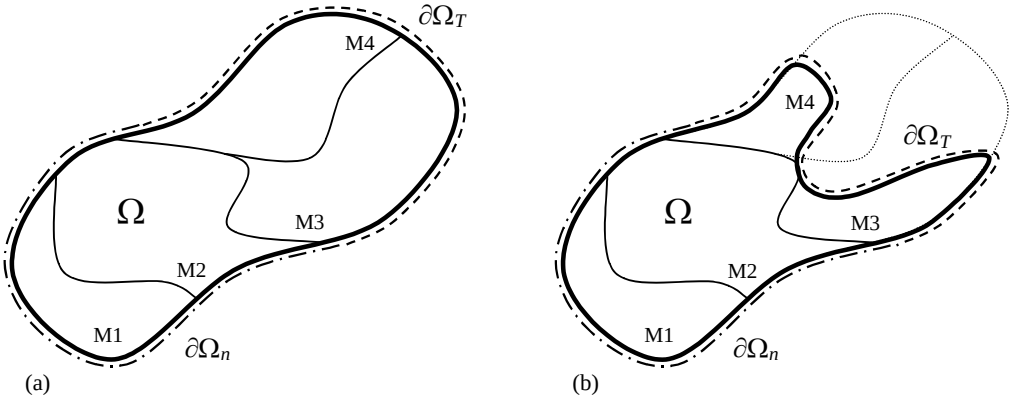

Figure 1. Schematic of the general problem.

Our purpose is to determine the location of the boundary $\partial\Omega_T$, and so the geometry of the volume Ω, matching a set of temperatures measured at certain points located inside the volume. Therefore, our general problem is an inverse geometry heat transfer problem where the observations are temperature measurements at points inside the volume and the unknown is the geometry of the volume where the problem is defined.

2.1. The direct heat transfer problem

The direct problem solution is a prerequisite for the solution of the inverse problem. Our direct problem is a steady-state heat transfer problem governed by

$$\boldsymbol{\nabla} \cdot (k \boldsymbol{\nabla} T) = 0 \qquad \forall \mathbf{x} \in \Omega, \tag{1}$$

where k is the temperature-dependent thermal conductivity, $\Omega \subset \mathbb{R}^{n_{\mathrm{dim}}}$ is a bounded domain with $1 \leq n_{\mathrm{dim}} \leq 3$, and $\partial\Omega$ is the smooth boundary of Ω.

Equation (1) is subjected to the following boundary conditions on $\partial\Omega_T$, $\partial\Omega_q$ and $\partial\Omega_c$, complementary parts of $\partial\Omega$ ($\partial\Omega_n = \partial\Omega_q \cup \partial\Omega_c$, $\partial\Omega_q \cap \partial\Omega_c = \varnothing$ and $\partial\Omega = \partial\Omega_T \cup \partial\Omega_n$, $\partial\Omega_T \cap \partial\Omega_n = \varnothing$):

- Dirichlet boundary condition on $\partial\Omega_T$:

$$T = T_w \qquad \forall \mathbf{x} \in \partial\Omega_T \ , \tag{2}$$

  where T_w is a given imposed temperature.
- Neumann boundary condition on $\partial\Omega_q$:

$$-k \ \boldsymbol{\nabla} T \cdot \mathbf{n} = q_w \qquad \forall \mathbf{x} \in \partial\Omega_q \ , \tag{3}$$

  where q_w is a given normal heat flux and $\mathbf{n}$ is the outward normal to the surface $\partial\Omega$.
- Robin boundary condition on $\partial\Omega_c$:

$$-k \ \boldsymbol{\nabla} T \cdot \mathbf{n} = h \ (T - T_\infty) \qquad \forall \mathbf{x} \in \partial\Omega_c \ , \tag{4}$$

  where h is the convective heat transfer coefficient and T_∞ is the ambient temperature.

The Galerkin finite element method [25, 26] is used to solve the direct heat transfer problem. Thus, we obtain the following system of equations

$$\left(\mathbf{K}^k + \mathbf{K}^c\right) \ \mathbf{T}^{FEM} - \mathbf{F} = \mathbf{0}, \tag{5}$$

where $\mathbf{T}^{FEM}$ is the vector of nodal temperatures, $\mathbf{K}^k$ is the conductivity matrix, $\mathbf{K}^c$ is the thermal convection matrix and $\mathbf{F}$ is the thermal load vector, given by

$$\widetilde{T} = \mathbf{N} \ \mathbf{T}^{FEM} \ , \tag{6}$$

$$\mathbf{K}^k = \int_\Omega \mathbf{B}^T \ \mathbf{k} \ \mathbf{B} \ dV \ , \tag{7}$$

$$\mathbf{K}^c = \int_{\partial\Omega_c} h \ \mathbf{N}^T \ \mathbf{N} \ dS \ , \tag{8}$$

$$\mathbf{F} = \int_{\partial\Omega_c} h \ \mathbf{N}^T \ T_\infty \ dS - \int_{\partial\Omega_q} \mathbf{N}^T \ q_w \ dS \ , \tag{9}$$

where $\widetilde{T}$ is the approximated temperature field, $\mathbf{N}$ is the finite element interpolation matrix, and $\mathbf{B}$ is the temperature-gradient interpolation matrix whose components are $B_{ij} = \dfrac{\partial N_j}{\partial x_i}$.

The equations are nonlinear because the thermal conductivity is temperature-dependent; therefore, it is necessary to solve them using an iterative technique.

3. FORMULATION OF THE INVERSE GEOMETRY PROBLEM

We consider our problem in finite-dimensional subspaces because we aim at obtaining practical applications. This means that not only the number of measurements is finite, but also the location of the unknown boundary $\partial\Omega_T$ is parametrized in order to obtain the approximate solution numerically.

Therefore, we parametrize the location of the unknown boundary $\partial\Omega_T$ by a set of n_p parameters $\mathbf{p} = (p_1, \ldots, p_{n_p})$, and we formulate the inverse problem as finding the geometry parameters $\mathbf{p}^*$ such that

$$\mathbf{p}^* = \arg \min_{\mathsf{p} \in \mathbb{R}^{n_p}} \mathcal{F}_{(\mathsf{p})} \tag{10}$$

where $\mathcal{F}_{(\mathsf{p})}$ is a function defined by the least-square error between the calculated and measured temperatures. Thus, $\mathcal{F}_{(\mathsf{p})}$ is given by

$$\mathcal{F}_{(\mathsf{p})} = \frac{1}{2} \left\| \mathbf{T}_{(\mathsf{p})} - \mathbf{T}^{Obs} \right\|^2 = \frac{1}{2} \sum_{i=1}^{n_{obs}} \left[\widetilde{T}_{\left(\mathsf{x}_i^{Obs}, \mathsf{p}\right)} - T_i^{Obs} \right]^2 , \tag{11}$$

where T_i^{Obs} is the temperature measured at point $\mathbf{x}_i^{Obs}$, $\widetilde{T}_{\left(\mathsf{x}_i^{Obs}, \mathsf{p}\right)}$ is the temperature calculated by the finite element model using the geometry parameters $\mathbf{p}$, and n_{obs} is the number of observations.

It is well-known that inverse problems are typically ill-posed in the sense that small observation perturbations can lead to big errors in the solution [6, 7]. Therefore, it is necessary to apply regularization methods in order to guarantee a stable solution. Several regularization methods have been used in the literature, and iterative regularization appears to be one of the most efficient approaches for the construction of stable algorithms for solving nonlinear inverse problems [7]. Among this class of methods, we use the iteratively regularized Gauss Newton method.

3.1. Iteratively regularized Gauss-Newton method

We use a discrete scheme of the interatively regularized Gauss-Newton method [8, 9, 10, 11], whose iterative solution is defined by:

$$\begin{aligned} {}^{GN}\mathbf{p}^{Iter+1} = \mathbf{p}^{Iter} + \Big[\mathbf{DT}^T_{(\mathsf{p}^{Iter})} \, \mathbf{DT}_{(\mathsf{p}^{Iter})} \; + \; \alpha_{Iter} \, \mathbf{L}^T \, \mathbf{L} \Big]^{-1} \\ \cdot \Big[\mathbf{DT}^T_{(\mathsf{p}^{Iter})} \, \mathbf{\Delta T}^{Obs}_{(\mathsf{p}^{Iter})} + \alpha_{Iter} \, \mathbf{L}^T \, \mathbf{L} \, \left(\mathbf{p}^{\triangle} - \mathbf{p}^{Iter} \right) \Big] \end{aligned} \tag{12}$$

where $Iter$ denotes the iteration number; $\mathbf{DT}_{(\mathsf{p})}$ is the sensitivity matrix; $\mathbf{L}$ is some regularization matrix; $\mathbf{\Delta T}^{Obs}_{(\mathsf{p})}$ is a vector whose components are $\left[T_i^{Obs} - \widetilde{T}_{\left(\mathsf{x}_i^{Obs}, \, \mathsf{p}\right)} \right]$ with $i = 1, n_{obs}$; $\mathbf{p}^{\triangle}$ is an a priori suitable approximation of the unknown set of parameters; and $\alpha_{Iter} > 0$ is the regularization parameter.

Further, the solution calculated with the iteratively regularized Gauss-Newton method, ${}^{GN}\mathbf{p}^{Iter+1}$, is used to update $\mathbf{p}^{Iter}$ as follows

$$\mathbf{p}^{Iter+1} = \mathbf{p}^{Iter} + \beta^{Iter} \, \left(\, {}^{GN}\mathbf{p}^{Iter+1} - \mathbf{p}^{Iter} \right) \tag{13}$$

where $\beta^{Iter} > 0$ is a step length such that

$$\mathcal{F}^*_{(\mathsf{p}^{Iter+1})} < \mathcal{F}^*_{(\mathsf{p}^{Iter})} \ , \tag{14}$$

with

$$\mathcal{F}^*_{(\mathsf{p})} = \frac{1}{2} \left\| \ \mathbf{T}_{(\mathsf{p})} - \ \mathbf{T}^{Obs} \right\|^2 + \frac{1}{2} \alpha \left\| \ \mathbf{L} \ \left(\mathbf{p} - \mathbf{p}^{\triangle} \right) \right\|^2 . \tag{15}$$

The selection of a step length makes sense due to the highly non-linear nature of the function $\mathcal{F}^*_{(\mathsf{p})}$, in which case β^{Iter} is typically less than 1.00.

3.1.1. Evaluation of the sensitivity matrix. The sensitivity matrix components are the partial derivatives of the temperature with respect to the set of geometry parameters. We evaluate them using a "discretize-then-differenciate" approach [27], which means that we first discretize the temperature field and then we differentiate it by a finite difference approximation

$$\left. \frac{\partial T}{\partial p_j} \right|_{(\mathsf{x},\mathsf{p})} \approx \frac{\widetilde{T}(\mathsf{x},\{p_1,\ldots,p_j+\Delta p_j,\ldots,p_{n_p}\}) - \widetilde{T}(\mathsf{x},\{p_1,\ldots,p_j,\ldots,p_{n_p}\})}{\Delta p_j} \ . \tag{16}$$

Therefore, the sensitivity matrix can be written as

$$\mathbf{DT}_{(\mathsf{p})} = \begin{bmatrix} \mathbf{N}_{(\mathsf{x}_1^{Obs})} & \left. \frac{\partial \mathbf{T}}{\partial p_1} \right|^{FEM}_{(\mathsf{p})} & \cdots & \mathbf{N}_{(\mathsf{x}_1^{Obs})} & \left. \frac{\partial \mathbf{T}}{\partial p_{n_p}} \right|^{FEM}_{(\mathsf{p})} \\ & \vdots & \ddots & & \vdots \\ \mathbf{N}_{(\mathsf{x}_{n_{obs}}^{Obs})} & \left. \frac{\partial \mathbf{T}}{\partial p_1} \right|^{FEM}_{(\mathsf{p})} & \cdots & \mathbf{N}_{(\mathsf{x}_{n_{obs}}^{Obs})} & \left. \frac{\partial \mathbf{T}}{\partial p_{n_p}} \right|^{FEM}_{(\mathsf{p})} \end{bmatrix} \in \mathbb{R}^{n_{obs} \times n_p} \ , \tag{17}$$

where $\left. \frac{\partial \mathbf{T}}{\partial p_j} \right|^{FEM}_{(\mathsf{p})}$ are vectors of nodal sensitivities with respect to the parameter p_j, such that

$$\left. \frac{\partial T}{\partial p_j} \right|_{(\mathsf{x},\mathsf{p})} \approx \mathbf{N}_{(\mathsf{x})} \ \left. \frac{\partial \mathbf{T}}{\partial p_j} \right|^{FEM}_{(\mathsf{p})} \ . \tag{18}$$

The components of these nodal sensitivity vectors can be easily obtained from definition (16) because the finite element discretization support is the same as the one we use for the temperature field.

3.1.2. Evaluation of the regularization matrix. The regularization matrix $\mathbf{L}$ is the discrete form of some differential operators [28, 11]. We choose a combination of the identity matrix $\mathbf{I}$ and discrete approximations of derivative operators given by

$$\mathbf{L}^T \ \mathbf{L} = \sum_{k=0}^{2} w_k \ \mathbf{L}_k^T \ \mathbf{L}_k \ , \tag{19}$$

where

$$\mathbf{L}_0 = \mathbf{I} \in \mathbb{R}^{n_p \times n_p} \tag{20}$$

$$\mathbf{L}_1 = \begin{bmatrix} 1 & -1 & & \\ & \ddots & \ddots & \\ & & 1 & -1 \end{bmatrix} \in \mathbb{R}^{(n_p-1)\times n_p} \tag{21}$$

$$\mathbf{L}_2 = \begin{bmatrix} 1 & 2 & -1 & & \\ & \ddots & \ddots & \ddots & \\ & & 1 & 2 & -1 \end{bmatrix} \in \mathbb{R}^{(n_p-2)\times n_p} \tag{22}$$

and $w_k \geq 0$ are weighting factors such that $\sum_{k=0}^{2} w_k = 1$. In Section 5, we study the solution behavior on different regularization matrices.

3.1.3. Determination of the regularization parameter. The regularization parameter $\alpha_{Iter} > 0$ is a priori chosen such that

$$1 \geq \frac{\alpha_{Iter+1}}{\alpha_{Iter}} \geq r, \quad \lim_{Iter\to\infty} \alpha_{Iter} = 0 \tag{23}$$

with $r < 1$. This monotically decreasing sequence has as its first term the optimal regularization parameter for the Tikhonov regularization method [6]

$$\alpha_0 \sim \delta^{\frac{2}{2\nu+1}}, \quad \nu \in [1/2; 1] \tag{24}$$

where δ is called the noise level.

3.1.4. Convergence criterion. Due to the instability of ill-posed problems, the iteration must not be arbitrarily continued when iterative regularization methods are used. Instead, the iterative process must be stopped at the right iteration because only for an appropriate stopping iteration, a stable solution is yielded. As shown in Figure 2, while the observation function (Equation (11)) decreases as the number of iterations increases, the error in the parameters (assuming the real solution known) starts to increase after certain number of iterations. Therefore, a stopping rule must be properly chosen.

We use the discrepancy principle as a stopping rule [6], that is, the iterative process is repeated until the iteration $Iter_\delta$, such that

$$\left\| \mathbf{T}_{(\mathbf{p}^{Iter_\delta})} - \mathbf{T}^{Obs} \right\| \leq \tau\ \delta < \left\| \mathbf{T}_{(\mathbf{p}^{Iter})} - \mathbf{T}^{Obs} \right\| \qquad 0 \leq Iter < Iter_\delta\ , \tag{25}$$

for some $\tau > 1$.

The discrepancy principle is based on stopping as soon as the observation function is in the order of the noise level, which means that the best approximation one should expect is in the order of the data error.

3.2. The bound-constrained problem

We stated our inverse geometry problem as finding the location of the boundary $\partial\Omega_T$, which is parametrized by a set of parameters $\mathbf{p}$, such that a set of temperature measurements at points

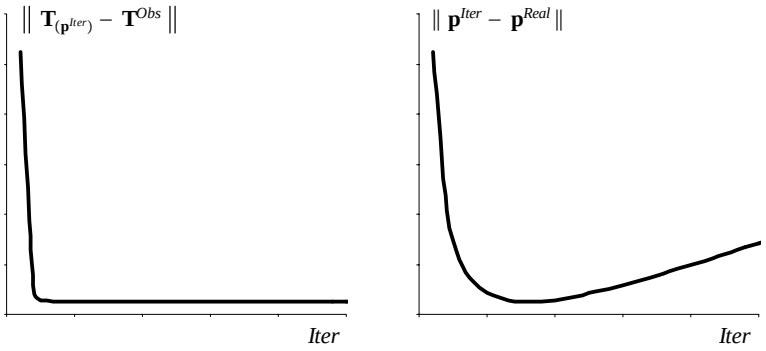

Figure 2. Typical error behaviour.

inside the volume is matched. But the location of the boundary $\partial\Omega_T$ may be subjected to some geometry restrictions, typically the thermally unloaded geometry bounds. These geometry restrictions can be expressed as geometry parameters bounds depending on the parametrization adopted.

Consequently, as Equation (12) has the following variational form

$$\mathcal{F}^{Iter}_{(\mathsf{p})} = \frac{1}{2}\left\|\mathbf{DT}_{(\mathsf{p}^{Iter})}\ \left(\ \mathbf{p}-\mathbf{p}^{Iter}\right) - \mathbf{\Delta T}^{Obs}_{(\mathsf{p}^{Iter})}\right\|^2 + \frac{1}{2}\alpha\left\|\mathbf{L}\ \left(\ \mathbf{p}-\mathbf{p}^{\Delta}\right)\right\|^2\ , \tag{26}$$

we reduce the original problem to a bound-constrained problem

$$\begin{aligned} &\min_{\mathsf{p}\in\mathbb{R}^{n_p}}\ \mathcal{F}^{Iter}_{(\mathsf{p})} \\ &\text{subject to}\ \ g^k_{(\mathsf{p})} \le 0 \quad k=1,n_p \end{aligned} \tag{27}$$

where $g^k_{(\mathsf{p})} = p_k - p^{max}_k$ are the geometry parameters inequality constraint conditions.

The Lagrange multiplier method [29] is used to convert the constraint minimization problem into a simpler problem, such that

$$\mathbf{p}^{Iter+1} = \arg\ \min_{\mathsf{p}\in\mathbb{R}^{n_p}}\ \left(\mathcal{F}^{Iter}_{(\mathsf{p})} + \lambda_k\ g^k_{(\mathsf{p})}\right) \tag{28}$$

where λ_k are the Lagrange multipliers.

Therefore, Equation (12) is rewritten as

$$\begin{aligned} &\begin{bmatrix} \mathbf{DT}^T_{(\mathsf{p}^{Iter})}\ \mathbf{DT}_{(\mathsf{p}^{Iter})}+\alpha\ \mathbf{L}^T\ \mathbf{L} & \mathbf{DG}^T_{(^r\mathsf{p})} \\ \mathbf{DG}_{(^r\mathsf{p})} & \mathbf{0} \end{bmatrix} \cdot \begin{bmatrix} \delta\mathbf{p} \\ \delta\boldsymbol{\lambda} \end{bmatrix} \\ &\qquad = \begin{bmatrix} \mathbf{DT}^T_{(\mathsf{p}^{Iter})}\ \mathbf{\Delta T}^{Obs}_{(\mathsf{p}^{Iter})}+\alpha\ \mathbf{L}^T\mathbf{L}\left(\ \mathbf{p}^{\Delta}-\mathbf{p}^{Iter}\right) - \mathbf{DG}^T_{(^r\mathsf{p})}\ {}^r\boldsymbol{\lambda} \\ -\mathbf{G}_{(^r\mathsf{p})} \end{bmatrix} \end{aligned} \tag{29}$$

where

$$\mathbf{DG}_{(\mathsf{p})} = \left.\frac{\partial g^k}{\partial p_j}\right|_{(\mathsf{p})}\ \in\ \mathbb{R}^{n_{ac}\times n_p}\ ;\ \forall\ g^k_{(\mathsf{p})} > 0\ , \tag{30}$$

r indicates the iteration of the optimization subproblem, and n_{ac} is the number of active constraints. Note that the dimension of the equation system to be solved changes as the number of active constraints changes.

The solution is iteratively updated as follows

$$^{r+1}\mathbf{p} = \mathbf{p}^{Iter} + \beta^{Iter}\ \delta\mathbf{p} \quad (31)$$

$$^{r+1}\boldsymbol{\lambda} = {}^{r}\boldsymbol{\lambda} + \beta^{Iter}\ \delta\boldsymbol{\lambda} \quad (32)$$

until a convergence criterion is satisfied. As a result, we obtain an acceptable feasible solution of $\mathbf{p}^{Iter+1}$ from this optimization subproblem.

3.3. The algorithm

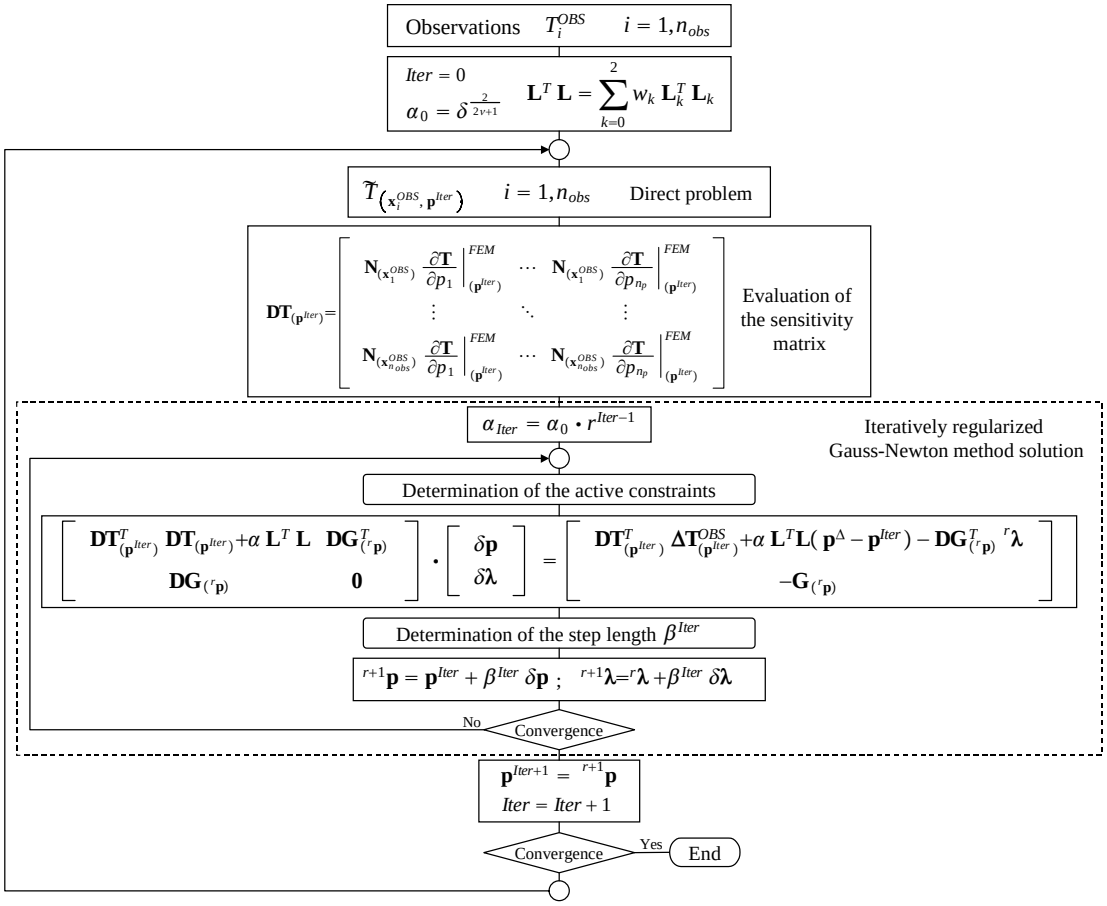

Figure 3. Iterative algorithm of the nonlinear inverse problem.

In Figure 3, we show the iterative algorithm of the nonlinear inverse problem. There are three different steps involved in the iterative process:

- the solution of the direct problem,
- the evaluation of the sensitivity matrix, which requires to solve the direct problem several times, and
- the determination of the iteratively regularized Gauss-Newton method solution of the bound-constrained problem, which also requires to solve the direct problem several times when the optimal step length is determined.

4. PARAMETRIZATION OF THE GEOMETRY

As stated in Section 3, the location of the unknown boundary $\partial\Omega_T$ is parametrized by $\mathbf{p} = (p_1, \ldots, p_{n_p})$, a set of n_p parameters. In addition, each parameter p_i has a base point with coordinates $\mathbf{BP}_{p_i}$ and a direction vector $\mathbf{DV}_{p_i}$; therefore, the definition of the unknown boundary is given by

$$\mathbf{SP}_{p_i} = \mathbf{BP}_{p_i} + p_i \, \mathbf{DV}_{p_i} \ . \tag{33}$$

Figure 4 shows an example of a set of base points and direction vectors which are used to describe the location of the unknown boundary $\partial\Omega_T$. Note that the selection of their location and orientation clearly depends on the geometry of each problem.

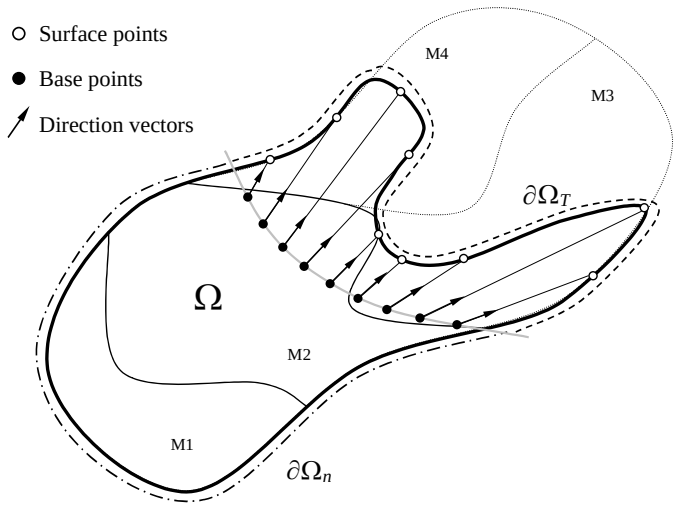

Figure 4. Schematic of the geometry parametrization.

Hence, given a set of surface points, the location of the unknown boundary $\partial\Omega_T$ is interpolated with a smooth function. We consider radial basis functions (RBFs) because they impose few restrictions on the geometry of the interpolation points which do not need to lie on a regular grid, and because they provide a smooth interpolation [12, 13, 14, 15, 16, 17]. Therefore, the direct heat transfer problem domain is perfectly defined.

Finally, since the direct problem must be solved several times for each inverse problem iteration, we use remeshing techniques in order to discretize each different geometry.

4.1. Radial Basis Functions

The problem consists in finding an interpolation function $\Phi(\mathbf{x})$ given a set of n_{sp} points on the unknown boundary $\partial\Omega_T$ (where $\Phi = 0$) and a set of n_{ip} points inside the volume Ω (where $\Phi < 0$). For this purpose, we choose RBFs defined by

$$\Phi(\mathbf{x}) = q(\mathbf{x}) + \sum_{i=1}^{n} \alpha_i \; R_{(\|\mathsf{x}-\mathsf{x}^i\|)} \tag{34}$$

where $n = n_{sp} + n_{ip}$; $q_{(\mathsf{x})}$ is a low degree polynomial; α_i are real numbers; and R is the basis function [12, 13, 14, 19] of which some examples are given below

1. Biharmonic spline, $R_{(r)} = r$.
2. Thin plate spline, $R_{(r)} = r^2 \; log(r)$.
3. Gaussian, $R_{(r)} = e^{-cr^2}$.
4. Triharmonic spline, $R_{(r)} = r^3$.
5. Triharmonic thin plate spline, $R_{(r)} = r^4 \; log(r)$.
6. Multiquadratic, $R_{(r)} = \sqrt{r^2 + c^2}$.
7. Exponential, $R_{(r)} = e^r$.

Among them, we use thin plate spline functions on $\mathbb{R}^2$ defined by

$$R_{(r)} = r^2 \; log(r) \tag{35}$$

$$q_{(\mathsf{x})} = q_{(x_1,x_2)} = d_0 + d_1 \; x_1 + d_2 \; x_2 \; . \tag{36}$$

As $\Phi(\mathbf{x})$ is chosen from the Beppo-Levi space of distributions on $\mathbb{R}^2$ with square integrable second derivative, some conditions must be imposed on α_i

$$\sum_{i=1}^{n} \alpha_i = \sum_{i=1}^{n} \alpha_i \; x_1^i = \sum_{i=1}^{n} \alpha_i \; x_2^i = 0 \; . \tag{37}$$

Therefore, the coefficients α_i and d_j are obtained from the following system of equations

$$\begin{bmatrix} \mathbf{A} & \mathbf{Q} \\ \mathbf{Q}^T & \mathbf{0} \end{bmatrix} \begin{pmatrix} \boldsymbol{\alpha} \\ \mathbf{d} \end{pmatrix} = \begin{pmatrix} \boldsymbol{\Phi} \\ \mathbf{0} \end{pmatrix} \tag{38}$$

where

$$\mathrm{A}_{ij} = \left\|\mathbf{x}^i - \mathbf{x}^j\right\|^2 \; log(\left\|\mathbf{x}^i - \mathbf{x}^j\right\|) \quad , \quad \mathbf{A} \in \mathbb{R}^{n\times n}; \tag{39}$$

$$\mathbf{Q} = \begin{bmatrix} 1 & x_1^1 & x_2^1 \\ \vdots & \vdots & \vdots \\ 1 & x_1^n & x_2^n \end{bmatrix} \in \mathbb{R}^{n\times 3}; \tag{40}$$

$$\boldsymbol{\alpha}^T = \begin{pmatrix} \alpha_1 & \cdots & \alpha_n \end{pmatrix} \in \mathbb{R}^n; \tag{41}$$

$$\mathbf{d}^T = \begin{pmatrix} d_0 & d_1 & d_2 \end{pmatrix} \in \mathbb{R}^3; \tag{42}$$

$$\boldsymbol{\Phi}^T = \begin{pmatrix} \Phi_{(\mathsf{x}^1)} & \cdots & \Phi_{(\mathsf{x}^n)} \end{pmatrix} \in \mathbb{R}^n \; . \tag{43}$$

Note that $\Phi_{(\mathsf{x}^i)}$ will be equal to zero except for the n_{ip} interior points.

4.2. Remeshing algorithm

As we focus on bidimensional problems, we implemented the following simple but effective remeshing algorithm:

1. The starting point is a structured mesh of quadrilateral elements, where different materials may be defined. According to the definition of the interpolation function $\Phi(\mathbf{x})$, there will be some nodes located inside the volume Ω, where $\Phi < 0$, and some located outside, where $\Phi > 0$. Remember that the unknown boundary $\partial\Omega_T$ is defined as $\Phi = 0$.
2. All the elements with three or four nodes inside the volume Ω ($\Phi < 0$) remain in the mesh (Step 1 of Figure 5).
3. A set of "boundary nodes" is defined. These nodes are the white ($\Phi < 0$) and grey ($\Phi > 0$) nodes of Figure 5.
4. The nodes that belong to the set of "boundary nodes" and that are located outside the volume Ω ($\Phi > 0$) are collapsed generating triangular elements (Step 2 of Figure 5).
5. Each node that belongs to the set of "boundary nodes" is moved to the nearest point of the unknown boundary $\partial\Omega_T$ (Step 3 of Figure 5). The nearest point is calculated solving the following non-linear optimization problem:

$$\min_{\mathbf{x}} f(\mathbf{x}) = \frac{1}{2}\left\|\mathbf{x}-\mathbf{x}^{Node}\right\|^2 \tag{44}$$

$$\text{subject to } \Phi(\mathbf{x}) = 0 \tag{45}$$

where $\mathbf{x}^{Node}$ are the coordinates of the node that is being moved.

5. INDUSTRIAL APPLICATION

In this section, we develop the industrial application of estimating the location of the 1150°C isotherm in a blast furnace hearth, based on measurements of thermocouples located inside it.

Regarding the direct problem, we model a vertical section of the lining (Figure 6) with axisymmetric finite elements because the geometry of the blast furnace hearth is rotationally symmetric about an axis and is subjected to axisymmetric cooling conditions (Table I). The finite element mesh has around 5000 isoparametric elements depending on the geometry solved for each inverse problem iteration. Table II shows the temperature dependence of the hearth refractories thermal properties considered in the direct model.

Cooling zone	Convective cooling parameters	
Lower hearth spray	$h_{water}= 150\ \frac{W}{m^{2\circ}C}$	$T_{water}= 20°C$
Bottom cooling	$h_{air}= \left(152.5 - 169.9\frac{r}{r_{max}} + 45.3\left[\frac{r}{r_{max}}\right]^2\right)\frac{W}{m^{2\circ}C}$	$T_{air}= \left(26 + 22\frac{r}{r_{max}}\right)°C$

Table I. Cooling conditions.

Regarding the inverse geometry problem, there are 28 thermocouples located inside the blast furnace hearth section (as shown in Figure 6) so the number of observations (n_{obs}) is equal to

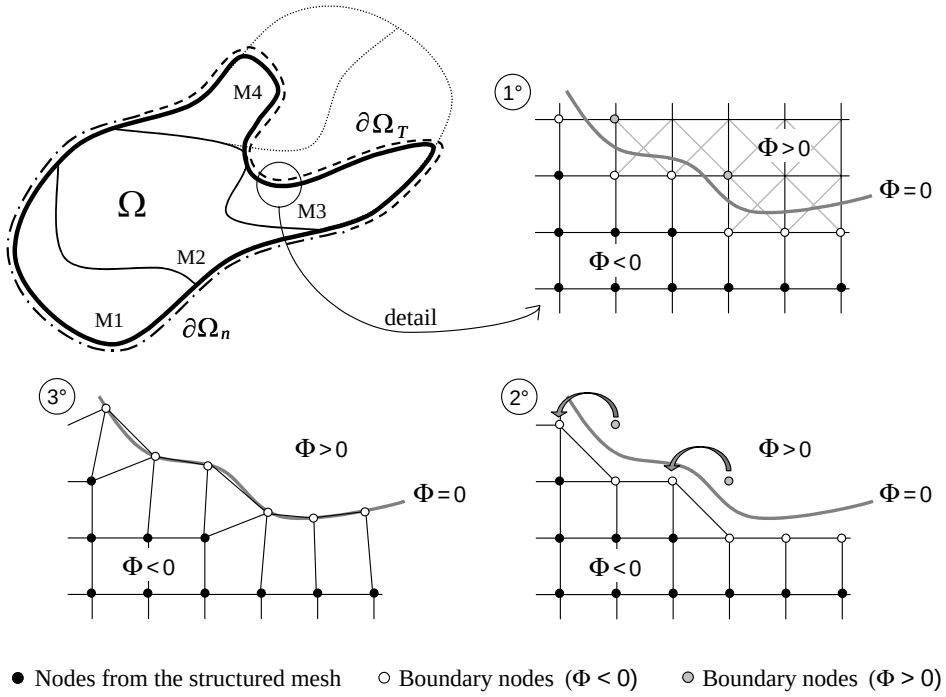

Figure 5. Schema of the remeshing algorithm.

Refractories	Thermal Conductivity	
SiC Castable	20.00W/mK	
Mortar	1.00W/mK	
Graphite EGF	T=303K	150.0W/mK
	T=773K	90.0W/mK
	T=1273K	60.0W/mK
Semi Graphite BC-30	T=293K	36.00W/mK
	T=473K	34.80W/mK
	T=673K	33.10W/mK
	T=873K	32.00W/mK
	T=1073K	31.50W/mK
Carbon BC-7S	T=873K	14.12W/mK
	T=1073K	14.99W/mK
	T=1273K	15.63W/mK
	T=1473K	16.09W/mK

Refractories	Thermal Conductivity	
SiC / Alumnina	7.20W/mK	
High Fired Super Duty	T=673K	1.300W/mK
	T=873K	1.400W/mK
	T=1073K	1.500W/mK
	T=1473K	1.600W/mK
EG Ramming	T=293K	25.00W/mK
	T=473K	20.00W/mK
	T=873K	11.00W/mK
	T=1273K	8.00W/mK
	T=1573K	7.00W/mK
Carbon BC-5	T=873K	16.96W/mK
	T=1073K	17.66W/mK
	T=1273K	18.13W/mK
	T=1473K	18.36W/mK

Table II. Material Properties.

28. The number of parameters used to parametrize the location of the unknown boundary (n_p) is chosen to be 7. As we said in the previous section, the selection of a set of base points and

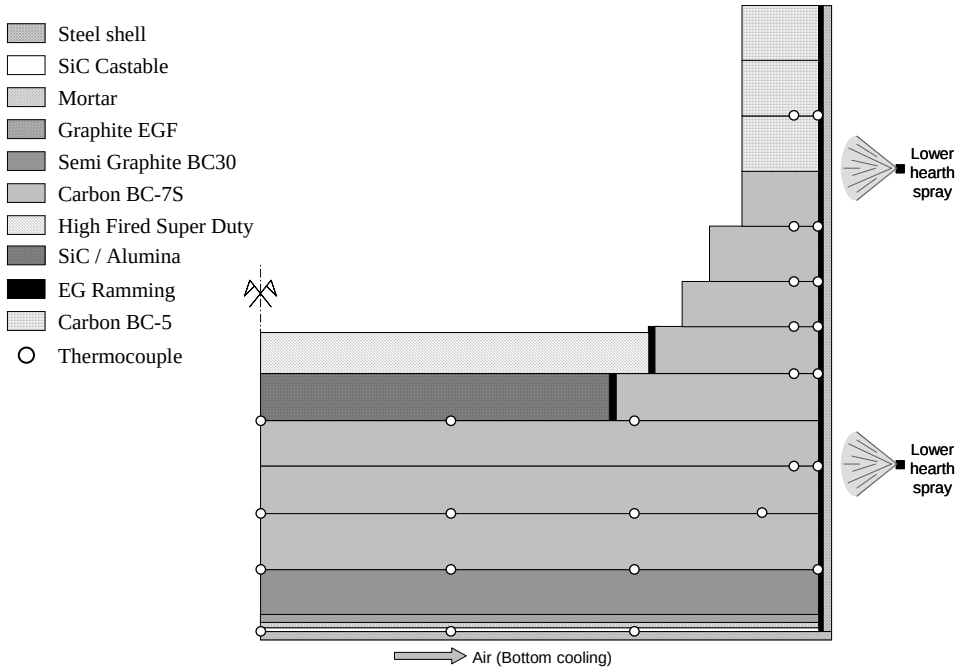

Figure 6. Vertical section of the blast furnace hearth.

direction vectors depends on the geometry of each problem. In our problem, we select them depending also on the position of the thermocouples.

Figure 7 shows the set of base points and direction vectors which are used to describe the location of the 1150°C isotherm, where the set of surface points is interpolated using thin plate spline RBFs (see Section 4.1).

In order to validate the solution of the algorithm against measurement uncertainties, we simulate measurements with different levels of noise following these steps:

1. We define a "real geometry" described by a set of geometry parameters $\mathbf{p}^{Real}$.
2. We calculate the temperature observations that correspond to the "real geometry", $\mathbf{T}^{Real}$, assuming error free measurements.
3. We simulate measurements with different levels of noise ($noise = 5\%, 10\%, 15\%$) as follows
$$T_i^{Obs} = T_i^{Real}\,(1 + \xi \cdot noise) \tag{46}$$
where $\xi \in [-1; +1]$ is a uniformly distributed random disturbance.

Then, we solve the inverse geometry heat transfer problem for each set of observations, using as initial guess the regularization geometry $\mathbf{p}^0 = \mathbf{p}^{\Delta}$, and we evaluate the following relative errors
$$\varepsilon_{obs} = \frac{\left\| \mathbf{T}_{(\mathbf{p}^{Iter})} - \mathbf{T}^{Obs} \right\|}{\|\mathbf{T}^{Obs}\|} \tag{47}$$

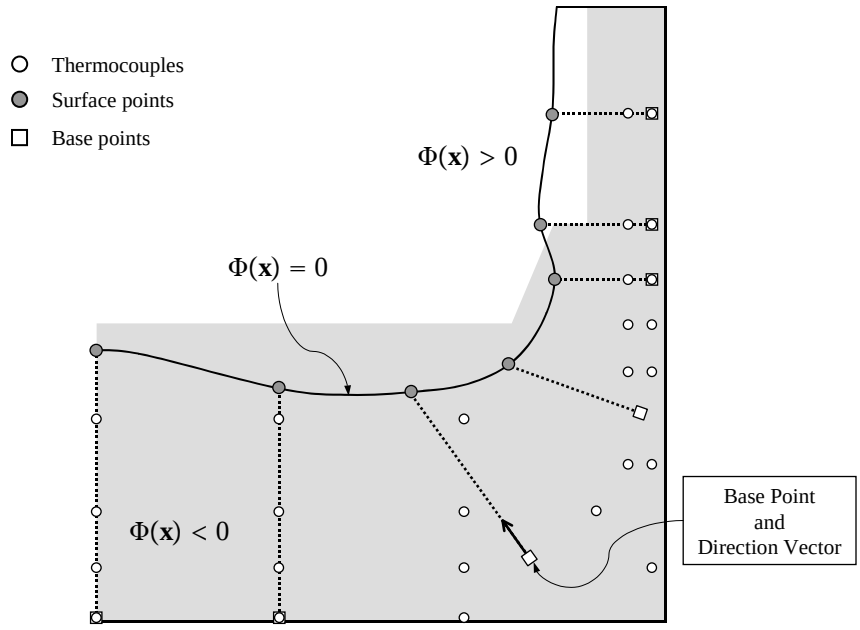

Figure 7. Parametrization of the unknown boundary location.

$$\varepsilon_{geom} = \frac{\left\| \mathbf{p}^{Iter} - \mathbf{p}^{Real} \right\|}{\|\mathbf{p}^{Real}\|} \ . \tag{48}$$

Finally, we focus on three aspects of the problem:

- The determination of the optimal regularization matrix for a problem with no geometry restrictions.
- The algorithm behavior when the problem is subjected to some geometry restrictions.
- The error behavior of the solution.

5.1. Determination of the optimal regularization matrix

We study the behavior of the algorithm on different regularization matrices. For this purpose, we propose five regularization matrices as linear combinations of $\mathbf{L}_0$, $\mathbf{L}_1$, $\mathbf{L}_2$ (Equation 19) and solve the inverse geometry heat transfer problem for each case, assuming a problem with no geometry restrictions.

Tables III, IV, V and VI show the relative errors (ε_{obs} and ε_{geom}) and the number of iterations required to solve the problem for each set of weighting factors (w_0, w_1, w_2) and for each noise level.

Analyzing these results, we conclude that:

- As is expected, the error on the estimated geometry, ε_{geom}, increases as the *noise* increases.

Case	w_0	w_1	w_2	ε_{obs} [%]	ε_{geom} [%]	Iter
1	1.00	0.00	0.00	0.164	0.455	4
2	0.00	1.00	0.00	0.162	0.397	4
3	0.00	0.00	1.00	0.151	0.352	4
4	0.00	0.50	0.50	0.156	0.373	4
5	0.50	0.50	0.00	0.188	0.537	4
6	0.50	0.00	0.50	0.187	0.513	4

Table III. Problem with no geometry restrictions - *noise* = 0%.

Case	w_0	w_1	w_2	ε_{obs} [%]	ε_{geom} [%]	Iter
1	1.00	0.00	0.00	2.698	4.317	3
2	0.00	1.00	0.00	3.041	4.816	3
3	0.00	0.00	1.00	2.925	2.807	3
4	0.00	0.50	0.50	3.666	4.631	3
5	0.50	0.50	0.00	2.729	4.395	3
6	0.50	0.00	0.50	3.647	4.571	3

Table IV. Problem with no geometry restrictions - *noise* = 5%.

Case	w_0	w_1	w_2	ε_{obs} [%]	ε_{geom} [%]	Iter
1	1.00	0.00	0.00	6.267	11.938	3
2	0.00	1.00	0.00	6.228	11.686	3
3	0.00	0.00	1.00	7.009	7.760	3
4	0.00	0.50	0.50	5.074	17.152	3
5	0.50	0.50	0.00	7.483	12.266	3
6	0.50	0.00	0.50	6.485	12.840	3

Table V. Problem with no geometry restrictions - *noise* = 10%.

Case	w_0	w_1	w_2	ε_{obs} [%]	ε_{geom} [%]	Iter
1	1.00	0.00	0.00	5.216	13.638	3
2	0.00	1.00	0.00	4.736	9.639	3
3	0.00	0.00	1.00	5.055	8.311	3
4	0.00	0.50	0.50	5.347	8.854	3
5	0.50	0.50	0.00	4.632	11.424	3
6	0.50	0.00	0.50	5.160	10.417	3

Table VI. Problem with no geometry restrictions - *noise* = 15%.

- The algorithm is equally stable for different regularization matrices when measurements have a low level of noise because ε_{geom} remains stable in all cases (Table IV).
- The optimal regularization matrix appears to be $(0.00, 0.00, 1.00)$ because the solutions have the lowest errors on the estimated geometry, ε_{geom}, particularly when measurements have a high level of noise (Tables V and VI).
- Even though 15% is a high level of noise, the geometry is estimated with good accuracy

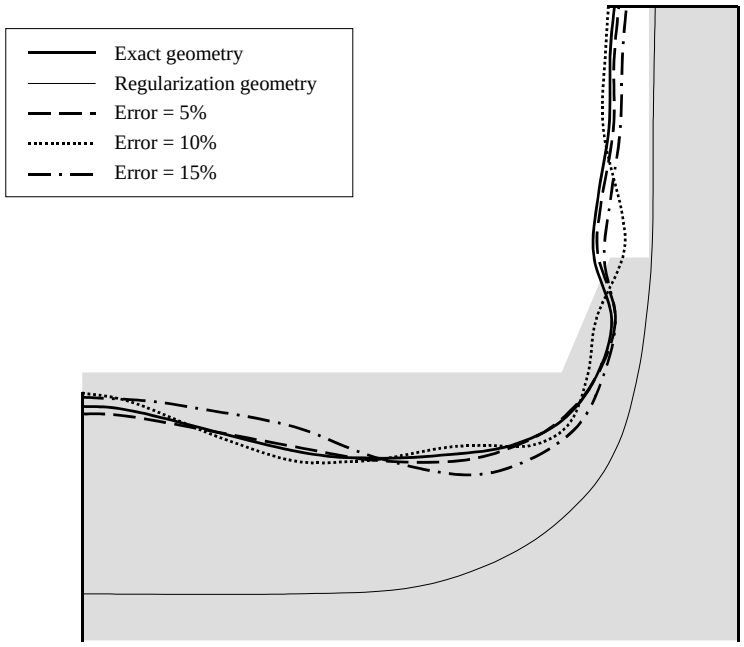

Figure 8. Estimated geometry for different levels of noise, using the optimal regularization matrix.

in the context of the industrial application (Figure 8).

5.2. The bound-constrained problem

We also study the behavior of the algorithm on different regularization matrices but, as our aim is to consider the bound-constrained problem, we only analyze the noise level for which the iterative solution process yields unfeasible solutions due to its instability. This is the case of $noise = 10\%$.

Table VII shows the relative errors (ε_{obs} and ε_{geom}) and the number of iterations required to solve the bound-constrained problem for each set of weighting factors (w_0, w_1, w_2).

Case	w_0	w_1	w_2	ε_{obs} [%]	ε_{geom} [%]	Iter
1	1.00	0.00	0.00	7.496	9.855	4
2	0.00	1.00	0.00	7.353	7.198	4
3	0.00	0.00	1.00	6.630	5.798	3
4	0.00	0.50	0.50	7.161	5.094	5
5	0.50	0.50	0.00	7.914	8.063	4
6	0.50	0.00	0.50	7.236	5.759	5

Table VII. Problem with geometry restrictions - $noise$ = 10%.

Analyzing these results, we conclude that:

- The solution is clearly improved and stabilized for all the regularization matrices when the bound-constrained algorithm is used (Tables V and VII).
- The optimal regularization matrix appears to be $(0.00, 0.00, 1.00)$, as in the problem with no geometry restrictions.
- More iterations are needed to reach convergence, which is an expected conclusion because the constraints are iteratively imposed.
- The geometry is estimated with good accuracy in the context of the industrial application (Figure 9).

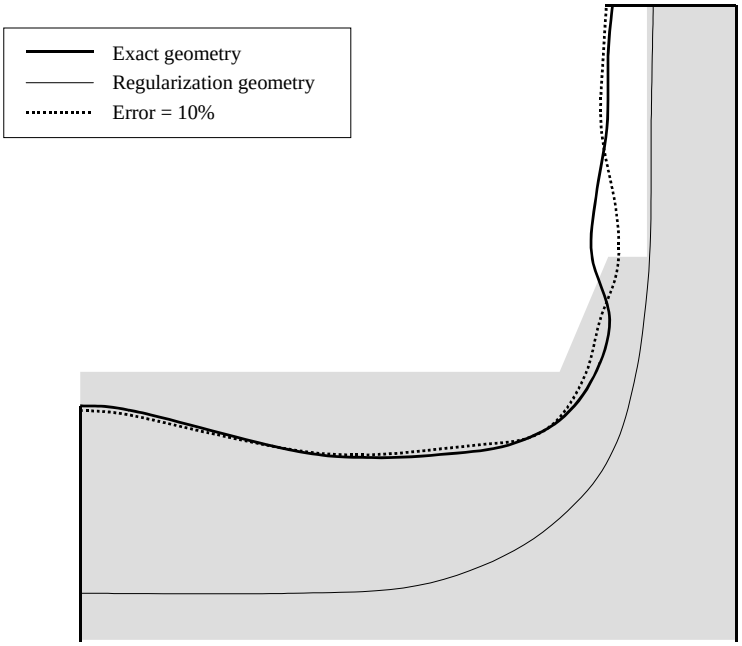

Figure 9. Geometry estimated by the bound-constrained algorithm, using the optimal regularization matrix..

5.3. Error behavior of the solution

We study the error behavior of the solution considering the optimal regularization matrix $(0.00, 0.00, 1.00)$ and the case of $noise = 10\%$, noise level for which the iterative solution process yields unfeasible solutions. Moreover, as this behavior depends on multiple factors, we divide the study in three parts.

In the first part of the study, we analyze the error behavior of the solution calculating an appropriate step length (Section 3.1) and considering no geometry restrictions. In the second part of the study, we also calculate an appropriate step length but we consider some geometry restrictions. Finally, in the third part of the study, we use a constant step length equal to 1.00 in order to evaluate the importance of calculating an appropriate step length.

Figures 10, 11 and 12 show the evolution of the relative errors (ε_{obs} and ε_{geom}) during the iterative process.

Analyzing these results, we conclude that:

- The typical instability of ill-posed problems, which cases ε_{geom} to increase after some iterations while ε_{obs} always decreases, clearly occurs in the first case (Figure 10). This confirms the use of the discrepancy principle as a stopping rule for the iterative process, as we explained in Section 3.1.4.
- The solution is strongly stabilized when the bound-constrained algorithm is used (Figure 11). Even in this case, the discrepancy principle is an efficient stopping rule for the iterative process.
- The behavior of the solution is not good when a constant step length equal to 1.00 is used (Figure 12). Therefore, as is expected, the selection of an appropriate step length makes sense due to the highly non-linear nature of the problem.

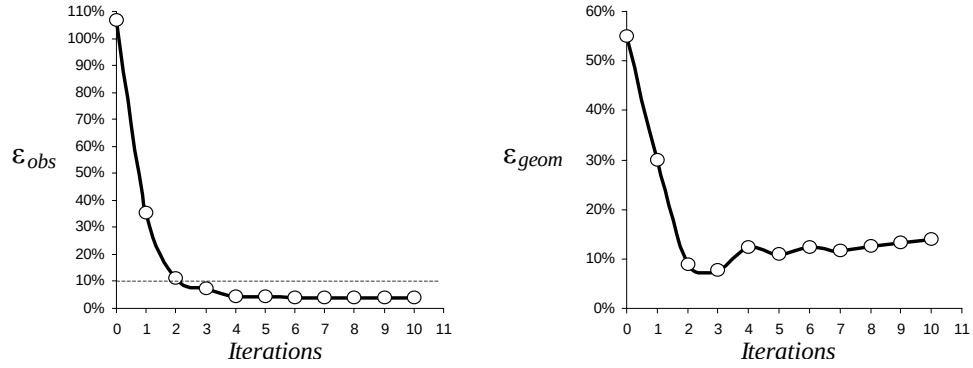

Figure 10. Error behavior of the solution, calculating an appropiate step length and considering no geometry restrictions.

6. CONCLUSIONS

We have developed an inverse geometry heat transfer model for estimating the location of the 1150°C isotherm in a blast furnace hearth. The observations of the inverse problem are temperature measurements at points inside the object and the unknown is the geometry of the volume where the problem is defined. We considered not only the problem with no geometry restrictions but also the bound-constrained problem. Due to the typical instability of ill-posed problems and the nonlineality of our inverse problem, we have used the iteratively regularized Gauss-Newton method.

The inverse geometry problem is based on a radial basis functions geometry representation. For this purpose, the location of the unknown boundary has been parametrized by a set of parameters and described with radial basis functions. We considered RBFs because they impose few restrictions on the geometry and because they provide a smooth interpolation.

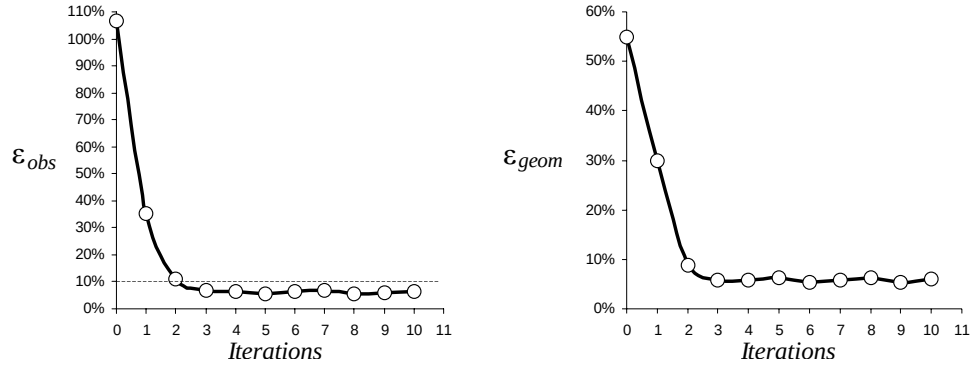

Figure 11. Error behavior of the solution, calculating an appropiate step length and considering some geometry restrictions.

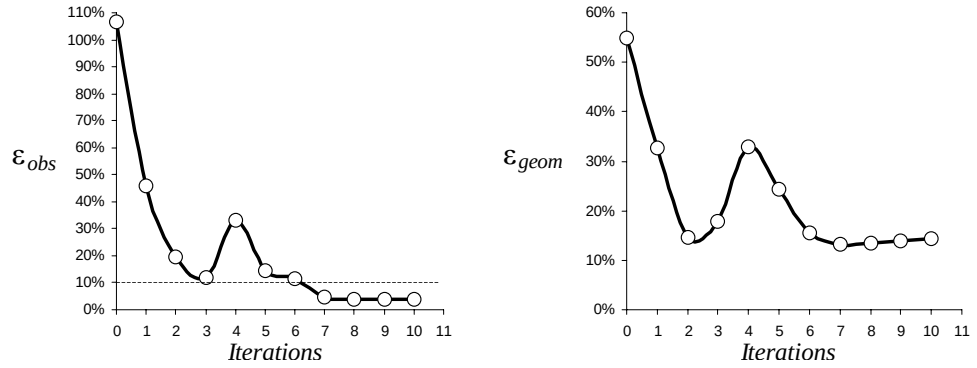

Figure 12. Error behavior of the solution, using a step length equal to 1.00 and considering no geometry restrictions.

The behavior of the algorithm on different regularization matrices has been studied analyzing its stability against simulated measurements with different levels of noise.

We can conclude, from the results of the analyzed cases, that the optimal regularization matrix appears to be $\mathbf{L}_2$ (the discrete approximation of the second derivative operator) for both the problem with no geometry restrictions and the bound-constrained problem. We also conclude that the solution is clearly improved and stabilized if the bound-constrained algorithm is used when the iterative solution process yields unfeasible solutions due to the instability of the problem.

On the basis of our numerical experimentation, we confirmed that a stopping rule for the iterative process must be used, and that the selection of an appropriate step length makes sense due to the highly non-linear nature of the problem.

Finally, as the geometry is estimated with good accuracy in the context of the industrial application, we conclude that the algorithm developed is a reliable tool for estimating the location of the 1150°C isotherm in a blast furnace hearth.

ACKNOWLEDGEMENT

We thankfully acknowledge the financial support and the information provided by SIDERAR (San Nicolás, Argentina).

REFERENCES

1. Wawrzynek A, Kogut M, Nowak A, Delpak R, Hu C-W. "Regularization method in geometrical inverse heat conduction problems-Preliminary report". ECCOMAS 2000. Barcelona, 2000.
2. Park HM, Shin HJ. "Shape identification for natural convection problems using the adjoint variable method". Journal of Computational Physics 2003; 186:198-211.
3. Kwag D-S, Park I-S, Kim W-S. "Inverse geometry problem of estimating the phase front motion of ice in a thermal storage system". Inverse Problems in Science and Engineering 2004; 12(1):1-15.
4. Huang C-H. "An inverse geometry problem in estimating frost growth on an evaporating tube". Heat and Mass Transfer 2002; 38:615-623.
5. Ganapathysubramanian S, Zabaras N. "A continuum sensitivity method for finite thermo-inelastic deformations with applications to the design of hot forming processes". Int. J. Numer. Meth. Engng 2002; 55:1391-1437.
6. Engl HW, Hanke M, Neubauer A. Regularization of inverse problems. Kluwer Academic Publishers, 1996.
7. Alifanov OM. Inverse heat transfer problems. Springer-Verlag, 1994.
8. Kaltenbacher B. "On convergence rates of some iterative regularization methods for an inverse problem for nonlinear parabolic equation connected with continuous casting of steel". J. Inv. Ill-Posed Problems 1999; 7(2):145-164.
9. Jin QN. "The analysis of a discrete scheme of the iteratively regularized Gauss-Newton method". Inverse Problems 2000; 16:1457-1476.
10. Kaltenbacher B, Neubauer A, Ramm AG. "Convergence rates of the continuous regularized Gauss-Newton method". J. Inv. Ill-Posed Problems 2002; 10(3):261-280.
11. Doicu A, Schreier F, Hess M. "Iteratively regularized Gauss-Newton method for atmospheric remote sensing". Computer Physics Communications 2002; 148:214-226.
12. Carr JC, Beatson RK, Cherrie JB, Mitchell TJ, Fright WR, McCallum BC. "Reconstruction and representation of 3D objects with radial basis functions". ACM SIGGRAPH 2001. Los Angeles, CA, 2001; 67-76.
13. Carr JC, Fright TJ, Batson RK. "Surface interpolation with radial basis functions for medical imaging". IEEE Transactions on Medical Imaging 1997; 20(Y):1-18.
14. Perrin F, Bertrand O, Pernier J. "Scalp current density mapping: value and estimation from potential data". IEEE Transactions on Biomedical Engineering 1987; BME-34(4):283-288.
15. Franke R. "Scattered data interpolation tests of some methods". Mathematics of Computation 1982; 38(157):181-200.
16. Kansa EJ. "Multiquadrics - A scattered data approximation scheme with applications to computational fluid-dynamics - II. Surface approximations and partial derivative estimates". Computers Math. Applic. 1990; 19(8/9):147-161.
17. Kansa EJ. "Multiquadrics - A scattered data approximation scheme with applications to computational fluid-dynamics - I. Solutions to parabolic, hyperbolic and elliptic partial differential equations". Computers Math. Applic. 1990; 19(8/9):127-145.
18. Turk G and O'Brien JF. "Variational implicit surfaces". Technical Report GIT-GVU-99-15, Georgia Institute of Technology, 1999.
19. Belytschko T, Parimi C, Moes N, Sukumar N, Usui S. "Structured extended finite element method for solids defined by implicit surfaces". Int. J. Numer. Meth. Engng 2003; 56:609-635.
20. Torrkulla J and Saxén H, "Model of the state of the blast furnace hearth", ISIJ International 2000; 40(5):438-447.
21. Sorli K and Skaar IM, "Monitoring the wear-line of a melting furnace". 3rd Int. Conference on Inverse Problems in Engineering 1999, Port Ludlow, WA, 1999.
22. Schulte M, Klima R, Ringel D, Voss M. "Improved wear-control at the blast furnace hearth by direct heat-flux measurements". Ironmaking Conference Proceedings 1998; 607-614.
23. Kurpisz K, "A method for determining steady state temperature distribution within blast furnace hearth lining by measuring temperature at selected points". Transactions ISIJ 1988; 28:926-929.
24. Gonzalez M, Goldschmit MB, Zubimendi JL, Gonzalez N, Ametrano R, Giandomenico F. "Inverse geometry problem of estimating the location of the 1150°C isotherm in a blast furnace hearth". Proceedings of the 4th IAS Ironmaking Conference 2003. San Nicolás, Argentina, 2003; 381-386.

25. Bathe KJ. Finite element procedures. Prentice-Hall, 1996.
26. Zienkiewicz OC, Taylor RL. The Finite Element Method (5th edn). Butterworth-Heinemann, 2000.
27. Appel JR and Gunzburger MD. "Sensitivity calculation in flows with discontinuities". Proc. 14th AIAA Applied Aerodynamics Conference New Orleans, USA 1996.
28. Brezinski C, Redivo-Zaglia M, Rodriguez G, Seatzu S. "Multi-parameter regularization techniques for ill-conditioned linear systems". Numer. Math. 2003; 94:203-228.
29. Luenberger DG. Linear and nonlinear programming. Addison Wesley, 1984.